ACS APPLIED MATERIALS & INTERFACES

Research Article

www.acsami.org

Facile Synthesis of Hierarchical Micro/Nanostructured MnO Material and Its Excellent Lithium Storage Property and High Performance as Anode in a MnO/$LiNi_{0.5}Mn_{1.5}O_{4-\delta}$ Lithium Ion Battery

Gui-Liang Xu,[†] Yue-Feng Xu,[†] Jun-Chuan Fang,[†] Fang Fu,[†] Hui Sun,[‡] Ling Huang,[†] Shihe Yang,[‡] and Shi-Gang Sun*,[†]

[†]State Key Laboratory of Physical Chemistry of Solid Surfaces, Department of Chemistry, College of Chemistry and Chemical Engineering, Xiamen University, Xiamen 361005, China

[‡]Department of Chemistry, The Hong Kong University of Science and Technology, Clear Water Bay, Kowloon, Hong Kong

Supporting Information

ABSTRACT: Hierarchical micro/nanostructured MnO material is synthesized from a precursor of $MnCO_3$ with olive shape that is obtained through a facile one-pot hydrothermal procedure. The hierarchical micro/nanostructured MnO is served as anode of lithium ion battery together with a cathode of spinel $LiNi_{0.5}Mn_{1.5}O_{4-\delta}$ material, which is synthesized also from the precursor of $MnCO_3$ with olive shape through a different calcination process. The structures and compositions of the as-prepared materials are characterized by TGA, XRD, BET, SEM, and TEM. Electrochemical tests of the MnO materials demonstrate that it exhibit excellent lithium storage property. The MnO material in a MnO/Li half cell can deliver a reversible capacity of 782.8 mAh g^{-1} after 200 cycles at a rate of 0.13 C, and a stable discharge capacity of 350 mAh g^{-1} at a high rate of 2.08 C. Based on the outstanding electrochemical property of the MnO material and the $LiNi_{0.5}Mn_{1.5}O_{4-\delta}$ as well, the MnO/$LiNi_{0.5}Mn_{1.5}O_{4-\delta}$ full cell has demonstrated a high discharge specific energy ca. 350 Wh kg^{-1} after 30 cycles at 0.1 C with an average high working voltage at 3.5 V and a long cycle stability. It can release a discharge specific energy of 227 Wh kg^{-1} after 300 cycles at a higher rate of 0.5 C. Even at a much higher rate of 20 C, the MnO/$LiNi_{0.5}Mn_{1.5}O_{4-\delta}$ full cell can still deliver a discharge specific energy of 145.5 Wh kg^{-1}. The excellent lithium storage property of the MnO material and its high performance as anode in the MnO/$LiNi_{0.5}Mn_{1.5}O_{4-\delta}$ lithium ion battery is mainly attributed to its hierarchical micro/nanostructure, which could buffer the volume change and shorten the diffusion length of Li^+ during the charge/discharge processes.

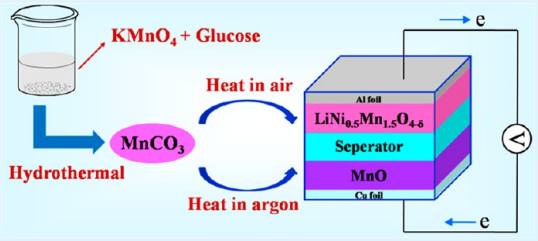

KEYWORDS: *hierarchical micro/nanostructured, olive shape, MnO, spinel $LiNi_{0.5}Mn_{1.5}O_{4-\delta}$, full cell, lithium ion batteries*

1. INTRODUCTION

Transition metal oxides (TMOs, M = Co, Ni, Cu, Fe, Mn) have been widely investigated as anode materials for lithium ion batteries (LIBs) in the past decades since reported by Tarascon et al. in 2000.[1−3] Among the TMOs, MnO anode has attracted more and more attention in recent years, because the MnO has a high theoretical capacity of 755.6 mAh g^{-1} that is twice the capacity of graphite, and a lower electromotive force (1.032 V vs Li/Li^+) than other TMO anodes such as Fe_2O_3, Co_3O_4, NiO, CuO, and so forth.[4−10] Such features result in a lower voltage polarization, and make the MnO more suitable as anode material for the next generation of LIBs than other TMOs. In addition, the relatively high voltage plateau (charge, ca. 1.2 V vs Li/Li^+; discharge, 0.5 V vs Li/Li^+) of the MnO can prevent the formation of lithium dendrite during charge/discharge and thus leads to a high safety. However, large volume changes during charge/discharge cycling and the low conductivity of MnO lead to a rapid capacity fading and a poor rate capability. Morphology control synthesis of the MnO materials has been considered as an efficient way to improve its electrochemical performance. In recent years, MnO materials of different structures such as core−shell nanorods,[11] nanotubes,[12] microspheres,[13] nanoplates,[14] nanoflakes,[15] and so forth have been synthesized, and they all demonstrated improved cycle performance to a certain degree when they are served as anode of LIBs. To the best of our knowledge, MnO anode with both long cycle performance (≥200 cycles) and high capacity (≥700 mAh g^{-1}) has been barely reported so far. Huang et al. has reported recently porous carbon-modified MnO disks[16] and mesoporous MnO/C networks;[17] the highest capacity of these anodes could reach 1224 mA h g^{-1} (much higher than the theoretical capacity of 755.6 mA h g^{-1} for MnO as anode) over 200 cycles. However, the capacity of these MnO materials presented a severe fading in the initial 50 cycles and then increased in the follow cycles of charge/discharge.

On the other hand, most of the previous works concerning TMOs anodes have only investigated their electrochemical properties in TMO/Li half cells. Only few examples applying

Received: April 13, 2013
Accepted: June 11, 2013
Published: June 11, 2013

   dx.doi.org/10.1021/am401355w | ACS Appl. Mater. Interfaces 2013, 5, 6316−6323

the TMOs into a full cell have been reported so far, which may be due to their high working voltage of the TMOs anode that will decrease the working voltage of the full cell. A full cell employing Fe_2O_3 as anode and $LiFePO_4$ as cathode was reported by Scrosati et al.[18] Though the capacity of the Fe_2O_3/$LiFePO_4$ battery is remarkable, the average working voltage of the battery is only 2.0 V. Tarascon et al. have reported a $LiMn_2O_4$/CoO full cell, whose average working voltage is slightly higher at 2.2 V.[1] Increase on the working voltage of full cell requires exploring anode material with low working voltage and cathode material with high working voltage. It is known that Ni-doped $LiMn_2O_4$ ($LiNi_{0.5}Mn_{1.5}O_4$) cathode has a high working voltage (ca. 4.7 V vs Li/Li^+) and a high specific capacity (148 mAh g^{-1}).[19] Although the MnO and $LiNi_{0.5}Mn_{1.5}O_4$ are both widely investigated anode and cathode materials in the past decades, their combination into a full cell has never been reported so far. An analogous lithium ion battery using $LiMn_2O_4$ as cathode and MnO_x/mesoporous carbon as anode has been reported By Lee et al. very recently. The capacity of the MnO_x/C anode decayed gradually from *ca.* 700 mAh g^{-1} to 500 mAh g^{-1} in 100 cycles, and the MnO_x/mesoporous carbon/$LiMn_2O_4$ full cell operates at an average working voltage of 3.3 V with a capacity of 105 mAh g^{-1}.[20]

In the current study, we have successfully developed a facile one-pot hydrothermal synthesis to prepare a precursor of hierarchical micro/nanostructured $MnCO_3$ with olive shape, from which both hierarchical micro/nanostructured MnO anode and spinel $LiNi_{0.5}Mn_{1.5}O_{4-\delta}$ cathode materials were obtained through a different calcination process. The electrochemical tests demonstrate that both the MnO and $LiNi_{0.5}Mn_{1.5}O_{4-\delta}$ materials possess excellent lithium storage properties owing to their unique hierarchical micro/nanostructures. The MnO in a MnO/Li half cell can deliver a reversible capacity of 782.8 mAh g^{-1} after 200 cycles at a rate of 0.13 C, and a stable reversible capacity of 350 mAh g^{-1} at a high rate of 2.08 C. A lithium ion battery using the MnO as anode and the $LiNi_{0.5}Mn_{1.5}O_{4-\delta}$ as cathode has been assembled, and it demonstrates a high discharge specific energy ca. 350 Wh kg^{-1} after 30 cycles at 0.1 C with an average working voltage at 3.5 V and a long cycle stability. The MnO/$LiNi_{0.5}Mn_{1.5}O_{4-\delta}$ full cell can maintain a discharge specific energy of 227 Wh kg^{-1} after 300 cycles at a higher rate of 0.5 C. Even at an extreme high rate of 20 C, it can still release a discharge specific energy of 145.5 Wh kg^{-1}. Considering the high specific energy, good cycleability, high rate performance, high safety, and low cost (natural abundance of Mn), the MnO/$LiNi_{0.5}Mn_{1.5}O_{4-\delta}$ full cell presents a promising potential for next generation of LIBs.

2. EXPERIMENTAL SECTION

2.1. Materials Synthesis. For the preparation of $MnCO_3$ hierarchical micro/nanostructure with olive shape, in a typical synthesis, 0.8 g of $KMnO_4$, 1 g of glucose, and 45 mL of deionized water were mixed under magnetic stirring. After 30 min stirring, the mixture was transferred and sealed in a 50 mL Teflon-lined autoclave, heated at 180 °C for 10 h, and finally cooled to room temperature. The precipitate was collected by centrifuge, washed alternately with deionized water and ethanol three times, and dried in vacuum oven at 80 °C overnight. MnO anode material was prepared by heating the as-prepared $MnCO_3$ at 550 °C for 4 h in high purity argon atmosphere. For the preparation of $LiNi_{0.5}Mn_{1.5}O_{4-\delta}$ (LNMO), $MnCO_3$ was heated at 400 °C for 5 h in air atmosphere to produce MnO_2. And then the MnO_2 was mixed with $LiOH{\cdot}H_2O$ and $Ni(NO_3)_2{\cdot}6H_2O$ in an ethanol solution. After the ethanol was stirred dry, a homogeneous gel was formed. The gel was heated at 800 °C for 20 h in air to prepare LNMO. For the synthesis of pure amorphous carbon, $KMnO_4$ was not added into the solution, the other condition was the same as that for MnO.

2.2. Materials Characterization. The morphologies and structures of the as-prepared samples were characterized by field emission scanning electron microscopy (HITACHI S-4800), transmission electron microscopy (FEI Tecnai-F30 FEG), and powder X-ray diffraction (XRD, Philips X'pert Pro Super X-ray diffractometer, Cu Kα radiation) measurements. The content of carbon in MnO was measured by TGA analysis of MnO in air atmosphere on the instrument of TG209F1. The specific surface area of the MnO anode and LNMO cathode were measured by the Brunauer–Emmett–Teller (BET) method using nitrogen adsorption and desorption isotherms on a Tristar3000 system.

2.3. Electrochemical Measurements. The MnO electrodes were prepared by spreading a mixture of 75 wt % MnO active material, 15 wt % acetylene black, and 10 wt % LA132 on to a copper foil current collector. The LNMO electrodes were prepared by spreading a mixture of 70 wt % LNMO active material, 20 wt % acetylene black, and 10 wt % LA132 on to an aluminum foil current collector. The as-prepared electrodes were dried at 80 °C in vacuum oven for 24 h and pressed under 10 MPa. For the half cell tests, the electrodes were measured by assembling them into coin cells (type CR2025) in an argon-filled glovebox with water and oxygen contents less than 0.5 ppm. Li foil was used as the counter electrode, and polypropylene (PP) film (Celgard 2400) as the separator. The electrolyte for LNMO cathode was made from $LiPF_6$ (1M) in a mixture of ethylene carbonate (EC)/dimethyl carbonate (DMC)/diethyl carbonate (DEC) in a volume ratio of 1:1:1, while for MnO anode 2 wt % vinylene carbonate (VC) was added as additive. The voltage ranges for testing MnO anode and LNMO cathode were 0.02–3.0 and 3.5–5.0 V, respectively. Electrochemical impedance spectroscopy (EIS) measurements were carried out using an electrochemical workstation (PARSTAT 2263, Princeton Applied Research) over a frequency range from 100 kHz to 1 Hz.

The diameter of the Cu and Al current collector used in the full cell was 12.5 mm and 12.0 mm, respectively, which were limited by the interval diameter of union (12.7 mm) in the Swagelok type cell (Figure S3, Supporting Information). In order to match the cathode/anode capacity, the mass ratio of cathode/anode material was adjusted at around 3.08/1. For instance, the active material loadings in the testing full cell were controlled at around 1.25 mg for MnO anode and 3.86 mg for LNMO cathode, respectively. Prior to full cell assembly, the MnO electrode was prelithiated by a surface treatment. This was performed by placing the electrode in direct contact with a Li foil wet by the electrolyte solution for 180 min. They were then assembled into a Swagelok type cell. The electrolyte was $LiPF_6$ (1M) in a mixture of ethylene carbonate (EC)/dimethyl carbonate (DMC)/diethyl carbonate (DEC) in a volume ratio of 1:1:1. The battery was cathode limited, and 1 C rate referring to the cathode weight was 148 mA g^{-1}. The charge/discharge voltage range for full cell test was 2.3–4.6 V.

3. RESULTS AND DISCUSSION

The thermal decomposition characteristic of the as-prepared $MnCO_3$ under N_2 atmosphere is investigated by thermogravimetric analysis (TGA) (Figure 1a). The $MnCO_3$ starts to decompose at ~255 °C and following by a significant weight loss (~ 36 wt %) at around 450 °C, which is slightly lower than the theoretical value of the weight loss for the decomposition of $MnCO_3$ into MnO (38.26 wt %). It indicates that there should be some carbon left over in the $MnCO_3$ due to glucose decomposition. The crystallographic structures of the as-synthesized samples are characterized by powder X-ray diffraction (XRD). The XRD patterns of the as-prepared $MnCO_3$, MnO, and LNMO are shown in Figure 2. They could be indexed to rhombohedral structure ($R\bar{3}c$) of $MnCO_3$ (JCPDS no. 00-044-1472), cubic MnO phase (JCPDS no. 01-089-4835), and cubic spinel $LiNi_{0.5}Mn_{1.5}O_4$ (JCPDS no. 01-

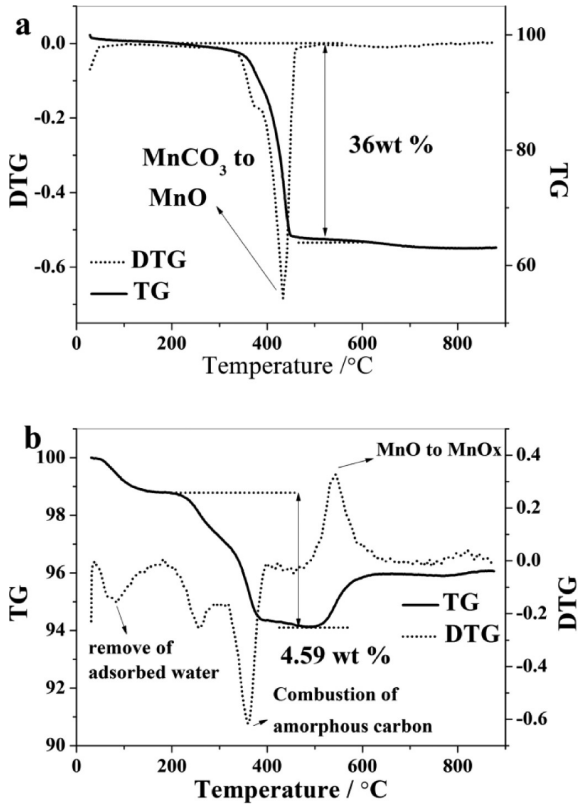

Figure 1. (a) TGA and DTG curve of $MnCO_3$ under N_2 atmosphere; (b) TGA and DTG curve of MnO material under air atmosphere.

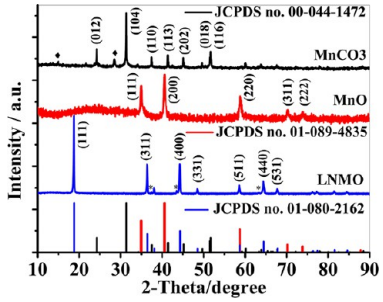

Figure 2. XRD patterns of $MnCO_3$, MnO, and LNMO and their standard XRD cards.

080-2162), respectively. The sharp and strong intensity of XRD peaks demonstrates the good crystallinity of the three samples. The minor peaks marked by diamond symbol in the XRD pattern of $MnCO_3$ are attributed to KMn_8O_{16}, which is generated because of the incomplete reduction between $KMnO_4$ and glucose. The broad diffraction peak at about 22° in the XRD pattern of MnO is ascribed to the existence of amorphous carbon. Pure amorphous carbon is prepared by hydrothermal reaction of glucose under 180 °C for 10 h followed by thermal annealing. Figure S1 in the Supporting Information shows the EIS spectra of commercial MnO, MnO/C and pure amorphous carbon electrodes. As shown, they all exhibit a depressed semicircle in the intermediate frequency region and short line in the low frequency range. It is well known that the semicircle in the intermediate frequency region is related to the charge-transfer impedance on the electrode/electrolyte interface, and the inclined line in the low frequency region corresponds to the lithium-diffusion process within electrodes. The electronic conductivity of electrode materials greatly affects their charge transfer resistance. The higher the electronic conductivity, the lower the charge transfer resistance. As can be seen, the transfer resistance of amorphous carbon electrode is very low, around 22 Ω, indicating a high conductivity. While the commercial MnO electrode presents a much higher transfer resistance of around 125 Ω, implying a low conductivity. In the case of MnO/C electrode, its transfer resistance is ca. 37 Ω, which is much lower than that of commercial MnO and slightly smaller than that of pure amorphous carbon. These results demonstrate that the conductivity of the MnO/C is much higher than that of commercial MnO and slightly lower than that of pure amorphous carbon. Therefore, by constructing the amorphous carbon with high conductivity in the MnO with microstructure, the conductivity of MnO could be increased. The content of the amorphous carbon has been determined by TGA analysis of MnO under air atmosphere (Figure 1b). The first weight loss from room temperature to 200 °C can be ascribed to the removal of adsorbed water, while the second weight loss in the temperature range of 200−450 °C is most likely due to the combustion of the amorphous carbon, and the weight increasing in the temperature range of 500−700 °C is related to the oxidation of MnO into MnO_x. The content of the amorphous carbon is thus determined as 4.59 wt %. The minor XRD peaks marked by asterisk symbol at 37.61°, 43.72°, and 63.23° in the XRD pattern of LNMO are assigned to NiO. The later is a common occurrence when the Ni content (x) in the $LiNi_xMn_{2-x}O_4$ spinel exceeds 0.2.[19]

The SEM image of the as-prepared $MnCO_3$ is illustrated in Figure 3a, which presents a uniform olive shape with a particle size ranging from submicrometer to ca. 3 μm. The formation of such olive morphology may come from the hydroxyls of glucose, which can function as a structure-directing agent during hydrothermal reaction.[21] The formation of $MnCO_3$ should be attributed to the oxidation of carbon into CO_3^{2-} that is inherited from glucose and the reduction of MnO_4^- into Mn^{2+}, and their further precipitation. The SEM image of MnO illustrated in Figure 3b clearly indicates that the olive shape is well preserved after calcination. From the SEM image of a broken particle (indicated by a red circle in Figure 3c), we can observe obviously that the olive MnO exhibits a hierarchical micro/nanostructure, which is composed of lots of tiny primary nanoparticles. This observation is further confirmed by the TEM image (up inset to Figure 3c), which presents interconnected primary nanoparticles with lots of pores. The size histogram (down inset to Figure 3c) indicates that the average primary particle size is ca. 11.6 nm. Such a small particle size of MnO could accommodate the volume changes and shorten the diffusion length of Li^+ during charge/discharge, and can therefore result in a good electrochemical performance of MnO. The formation of pores is ascribed to the release of CO_2 during decomposition of the $MnCO_3$. The nitrogen adsorption/desorption experiment reveals that the MnO has a specific surface area of 52.5 $m^2\ g^{-1}$ and a pore size distribution of 20 and 60 nm, confirming the porous structure of the MnO (Figure 3e, f). We can observe lots of micrometer-sized particles with olive shapes from the SEM image of the LNMO (Figure 3d). The TEM image inset to Figure 3d demonstrates that the LNMO is also composed of primary nanoparticles, presenting a hierarchical micro/nanostructure. The size of the primary nanoparticles in the LNMO product is measured to be around 20 nm. The interval between the nanoparticles

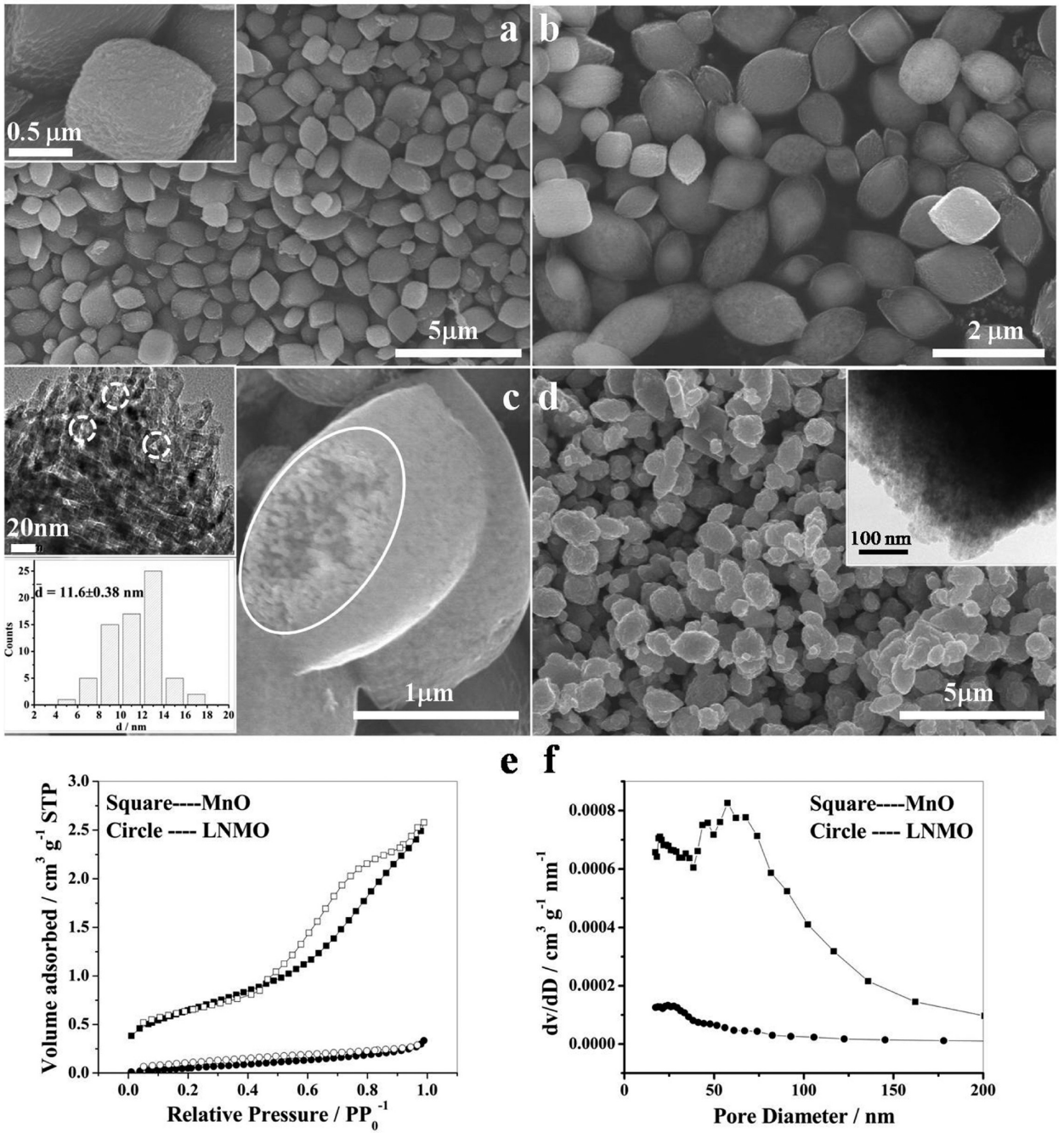

Figure 3. (a) SEM image of $MnCO_3$; (b) SEM image of MnO; (c) SEM image of an individual MnO particle; insets are the HR-TEM image (up) and size histogram (down) of MnO; (d) low magnification SEM image of LNMO, inset is its TEM image; (e) N_2 adsorption/desorption isotherms of MnO and LNMO, where solid refers to adsorption and hollow refers to desorption; and (f) pore size distribution of the MnO and LNMO.

demonstrates the porous structure of LNMO. The BET results illustrated in Figure 3e and f indicate that its pore size distribution is mainly at around 25 nm, and the specific surface area of the LNMO is 5.31 $m^2\ g^{-1}$.

In the current study, we apply the as-synthesized MnO as anode material and LNMO as cathode material to develop a MnO/LNMO lithium ion battery. The electrochemical performances of both MnO/Li and LNMO/Li half cell are investigated prior in order to get a thorough understanding of the feasibility of MnO/LNMO full cell. As can be seen in the first discharge curve of MnO anode (Figure 4a), the voltage drops to a plateau about 0.26 V from the open circuit potential and then decreases slowly to 0.02 V. During the initial charge process, the average charge plateau of the MnO is ca. 1.2 V, which is much lower than that of CoO (1.8 V),[22] Co_3O_4 (2.0 V),[23] Fe_2O_3 (1.6 V),[24] Fe_3O_4 (1.7 V),[25] NiO (1.9 V),[26] and CuO (2.1 V).[27] It can be clearly seen that the MnO displays a lower charge working voltage than most of the transition metal oxides reported until now, indicating a unique advantage of its application in LIBs. In the second cycle, the discharge plateau shifts to ca. 0.5 V, which is partially due to the improved kinetics and partially the deviation of the formation energy of the reactants from the products after the first insertion.[7] Figure 4b shows the differential capacity curves of MnO in the first and second cycle. In the first cycle, two small cathodic peaks appear at 1.89 and 1.57 V, and disappear in the second cycle,

dx.doi.org/10.1021/am401355w | ACS Appl. Mater. Interfaces 2013, 5, 6316−6323

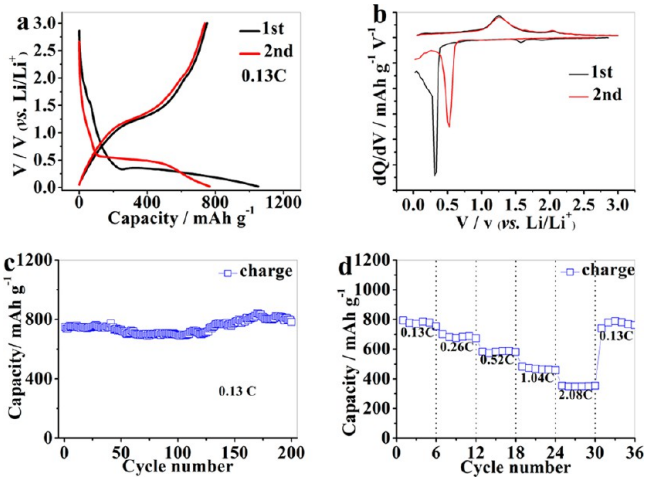

Figure 4. (a) Charge/discharge profiles of MnO/Li half cell and (b) the corresponding differential capacity curve at a 0.13 C rate; (c) cycling performance of MnO/Li half cell at a 0.13 C rate and (d) rate capability of MnO/Li half cell.

which may be attributed to the decomposition of minor impurities in the MnO.[11] The main cathodic peak at 0.26 V is due to the conversion reaction of MnO with lithium into Mn. In the anodic process, two peaks are recorded at 1.25 and 2.08 V, corresponding to the reoxidation of Mn^0 to Mn^{II} and the decomposition of gel/polymer-like layer, respectively.[11] The initial discharge capacity of MnO anode at a rate of 0.13 C (1 C = 755.6 mA g^{-1}) is 1051.4 mAh g^{-1}, and the initial charge capacity of the MnO anode is 749.8 mAh g^{-1}, leading to an initial Coulombic efficiency of 71.3% that is common for transition metal oxide anodes. The irreversible capacity is mainly ascribed to the decomposition of electrolytes to form a solid electrolyte interphase (SEI) layer and the further lithium storage via interfacial charging at the metal/Li_2O interface.[4,12−14] The irreversible capacity may not come from the amorphous carbon left over in the MnO. Considering its electrochemical performance shown in Figure S2 (Supporting Information) and the low content (4.59 wt %), the first irreversible capacity produced by the amorphous carbon is only 2 mAh g^{-1} and could be neglected.

The cycling performance of the MnO/Li half cell at 0.13 C is illustrated in Figure 4c. The MnO anode displays an excellent cycling performance, for which it can deliver a stable and reversible charge capacity ca. 782.8 mAh g^{-1} after 200 cycles of charge/discharge at 0.13 C. To the best of our knowledge, it is superior to most of the previous results reported concerning MnO-based anode.[7,9−14,28] The capacity of MnO anode exceeding its theoretical value may be attributed to the formation of polymeric gel-like layer on the surface of MnO electrode during charging/discharging as reported by Tarascon and et al.,[29] and have been also reported in other MnO anode materials.[17,28] The rate capability of MnO/Li half cell is also tested in order to investigate the fast charge/discharge properties of the MnO anode. As illustrated in Figure 4d, the charge/discharge rates are increased successively from 0.13 to 2.08 C for each 6 cycles. The average charge capacities for each 6 cycles at 0.13, 0.26, 0.52, and 1.04 C are 776.5, 683.9, 581.7, and 467.1 mAh g^{-1}, respectively. At a high rate of. 2.08 C, it can still deliver a reversible charge capacity of 350 mAh g^{-1}, which is almost the theoretical capacity of graphite. When the rate is decreased back to 0.13 C, almost 100% of the average charge capacity of the initial 6 cycles at 0.13 C has been recovered, illustrating an excellent rate capability.

The electrochemical performance of the LNMO cathode is also evaluated and shown in Figure 5. As can be seen in the

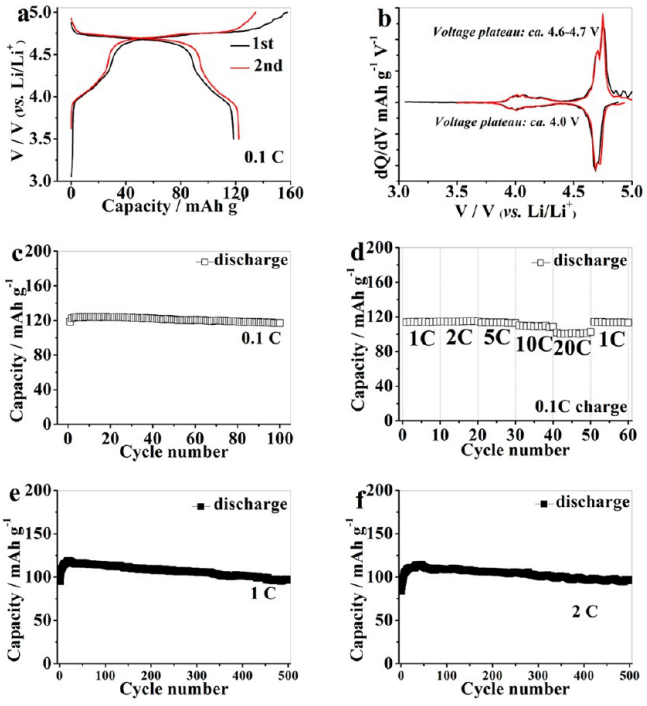

Figure 5. (a) Charge/discharge profiles of LNMO/Li half cell and (b) the corresponding differential capacity curve at a 0.1 C rate; (c) cycling performance of LNMO/Li half cell at a 0.1 C rate; (d) rate capability of LNMO/Li half cell (0.1 C charge, different rates discharge); cycling performance of LNMO/Li half cell at a rate of 1 C (e) and 2 C (f).

charge/discharge profiles of LNMO at 0.1 C (Figure 5a), the LNMO cathode has a main voltage plateau at ca. 4.7 V, associating with the oxidation of Ni^{2+} to Ni^{3+} and Ni^{3+} to Ni^{4+}.[30] A charge plateau at approximately 4.0 V is also observable, reflecting the redox reaction between Mn^{3+} and Mn^{4+} and affirming that the LNMO is in disordered structure with $Fd\bar{3}m$ space group. Its formation may be ascribed to the appearance of oxygen deficiency during high temperature calcination that would reduce a small fraction of Mn^{4+} to Mn^{3+}. These charge/discharge characteristics are in good accordance with its differential capacity curves displayed in Figure 5b. The initial charge capacity of the LNMO cathode at 0.1 C is 157.7 mAh g^{-1}, and the initial discharge capacity is 118.4 mAh g^{-1}, resulting in an initial Coulombic efficiency of 75.1%. The irreversible capacity is also attributed to the electrolyte decomposition. The cycling performance of the LNMO/Li half cell at 0.1 C is demonstrated in Figure 5c. As shown, the LNMO cathode can maintain a stable discharge capacity ca. 120 mAh g^{-1} in 100 cycles, indicating an excellent cycleability of the LNMO when served as cathode of LIBs. Figure 5d shows the rate performance of the LNMO cathode material charging at 0.1 C and discharging at rates ranging from 1 to 20 C and then back to 1 C. With increasing the discharge rates, the discharge capacities have little decrease from 1 to 10 C, the average discharge capacities at 1, 2, 5, and 10 C are 114.2, 114.7, 113.9, and 109.2 mAh g^{-1}, respectively. At an extremely high rate of 20 C, it can still deliver a capacity of 101.0 mAh g^{-1}, which is 88.4% of the average charge capacity at 1 C. When the rate is

decreased back to 1 C, a reversible discharge capacity of 113.7 mAh g^{-1} is measured, which is nearly 100% of the initial discharge capacity at 1 C. The LNMO also shows long cycleability at high rates. At a rate of 1 C (Figure 5e), after a few cycles of activation, the LNMO cathode material can maintain a reversible discharge capacity of 96.8 mAh g^{-1} after 500 cycles at 1 C rate. At a higher rate of 2 C, the LNMO could deliver 96.1 mAh g^{-1} after 500 cycles, indicating good cycle stability of LNMO cathode (Figure 5f). The increasing trend on capacity along with the cycle number is effectively more notable under high current densities. This should be attributed to the activation of the cell, that is, mass transfer under high current densities. The mass transfer is slower than the charge transfer under high current densities. Therefore, in the initial few cycles of charge/discharge, not enough active materials are involved in the charge/discharge process, leading to the low initial capacities. It will be more severe when increasing the current densities. After few cycles of activation, the capacities are gradually increased due to more and more active materials participating in the charge/discharge process. This phenomenon is common in the study of lithium ion batteries and can be seen in previously reported literature.[30,31] In addition, the electrochemical performance of the as-prepared LNMO cathode could be comparable with the results recently reported by Lou et al.[19] and Zhang et al.[30]

The structure stability of electrode materials has a great influence on their electrochemical performances. Once the structure is destroyed, the capacity of electrode materials will decay rapidly. The morphologies of MnO anode and LNMO cathode after charge/discharge are characterized by scanning electron microscopy. As shown in Figure 6a, the MnO anode

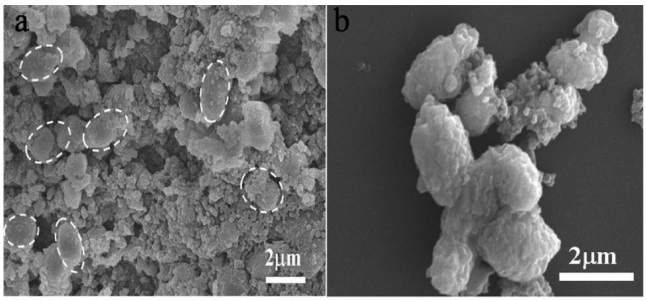

Figure 6. SEM images of the (a) MnO electrode after 200 cycles of charge/discharge at a rate of 0.13 C. (b) SEM image of LNMO electrode after 100 cycles of charge/discharge at a rate of 0.1 C.

after 200 cycles of charge/discharge at 0.13 C can maintain its hierarchical micro/nanostructure with the olive shape. The SEM image of the LNMO cathode material after 100 cycles of charge/discharge at 0.1 C is illustrated in Figure 6b. It also indicates clearly the conservation of the hierarchical structure with the olive shape. Such good structural durability should be responsible for their superb lithium storage performances.

Based on the excellent electrochemical performances of both MnO and LNMO in half cells, we use the as-synthesized MnO and LNMO materials to assemble a MnO/LNMO full cell. Since irreversible capacity of both the MnO anode and LNMO cathode are observed in the initial cycle, we take the second cycle (reversible process) to discuss the feasibility of the MnO/LNMO full cell. Figure 7a shows the second charge curve of the LNMO cathode and the second discharge curve of the MnO anode. The LNMO cathode possesses a charge capacity of

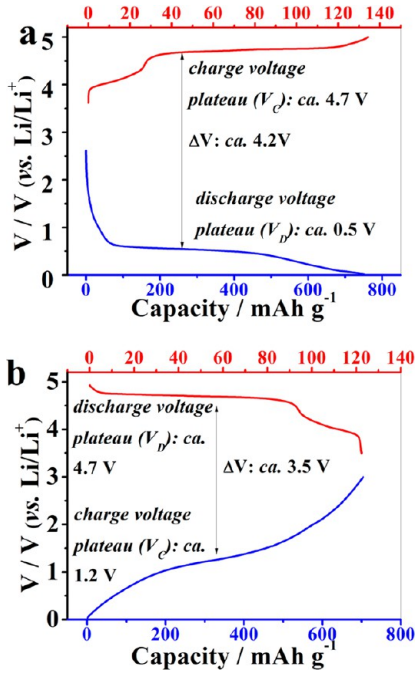

Figure 7. (a) Second charge curve of LNMO/Li half cell (red line) and second discharge curve of MnO/Li half cell (blue line); (b) second discharge curve of LNMO/Li half cell (red line) and the second charge curve of MnO/Li half cell (blue line).

134.3 mAh g^{-1} and a charge voltage plateau (V_C) at around 4.7 V. On the other hand, the MnO anode presents a discharge capacity of 751 mAh g^{-1} and a discharge plateau (V_D) at ca. 0.5 V. The specific energy (E) of a MnO/LNMO full cell could be therefore estimated by the equation below.[32]

$$E = C_{\text{cathode}}C_{\text{anode}}(V_{\text{cathode}} - V_{\text{anode}})/(C_{\text{cathode}} + C_{\text{anode}}) \quad (1)$$

where C indicates the theoretical capacity and V denotes the average working voltage. Using the data reported above, the MnO/LNMO full cell may deliver a charge capacity of 113.9 mAh g^{-1} with an average plateau at 4.2 V, and result in a theoretical charge specific energy ca. 478.5 Wh kg^{-1}. Figure 7b illustrates the second discharge curve of LNMO cathode and the second charge curve of MnO anode. Based on similar analysis to Figure 7a, the MnO/LNMO full cell could release a discharge capacity of 104.2 mAh g^{-1} with an average discharge plateau at ca. 3.5 V, resulting in a theoretical discharge specific energy ca. 364.7 Wh kg^{-1}. From these analyses based on individual behaviors of the MnO/Li and LNMO/Li half cell, it is obvious that the MnO/LNMO full cell possesses a great interest for its high theoretical specific energy and high output working voltage.

Prior to the MnO/LNMO full cell test, the MnO electrode is prelithiated by a surface treatment. This treatment could form extra Li_2O on the surface of the electrode, and improve the initial irreversible capacity loss. The MnO anode and LNMO cathode are then assembled into a well-known Swagelok type cell (Figure S3, Supporting Information). In our study, the amount of anode material is in excess to cathode material, the capacity of MnO anode is adjusted around twice that of LNMO cathode. Figure 8a illustrates the charge/discharge curves of the MnO/LNMO full cell at 0.1 C. In the first charge process, two main charge plateaus at ca. 3.72 and 4.5 V are observed; in the first discharge process, two main discharge plateaus at ca. 2.92

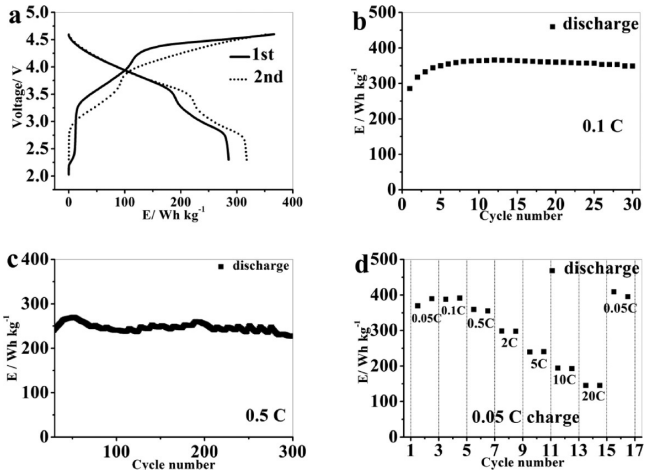

Figure 8. (a) Charge/discharge profiles and (b) cycling performance of the MnO/LNMO full cell at a rate of 0.1 C; (c) cycling performance of the MnO/LNMO full cell at a rate of 0.5 C; (d) the discharge specific energies of MnO/LNMO full cell at different rates (0.05 C charge).

and 3.75 V are also noticed (Figure S4, Supporting Information). In the subsequent second cycle, the charge voltage plateaus are shifted to lower potentials at ca. 3.3 and 4.1 V, resulting from the shift of discharge plateau of MnO anode in the initial two cycles. Based on the active mass of LNMO cathode, the initial charge specific energy is measured at 366.8 Wh kg^{-1}, and the initial discharge specific energy is thus 285.5 Wh kg^{-1}, together with an initial Coulombic efficiency of 77.8%.

Figure 8b reveals the corresponding cycling performance of the MnO/LNMO full cell at 0.1 C. It is clear that, after few cycles of activation, the cell could maintain a highly reversible and stable discharge specific energy ca. 350 Wh kg^{-1} after 30 cycles, which approaches the theoretical discharge specific energy (364.7 Wh kg^{-1}) of the full cell. We can observe a capacity increasing in the initial few cycles (Figure 8b). This capacity increase becomes more significant at high rate charge/discharge as shown in the cycling performance of the MnO/LNMO full cell at a higher rate of 0.5 C (Figure S5, Supporting Information). Such phenomenon may be attributed to the gradual decomposition of Li_2O that formed by the prelithiation and the inherent activation of LNMO cathode at high rate charge/discharge (Figure 5e and f). After 30 cycles activation, it can maintain a quite stable discharge specific energy around 250 Wh kg^{-1} in the followed 270 cycles at 0.5 C (Figure 8c). The high rate performance of the MnO/LNMO full cell is further evidenced by Figure 8d. The MnO/LNMO full cell is charged first at 0.05 C and then discharged at different rates by increasing gradually ranging from 0.05 to 20 C. The average discharge specific energies at 0.05 C, 0.1, 0.5, 2, 5, and 10 C are 379.5, 389.6, 357.3, 298.4, 240.2, and 193.6 Wh kg^{-1}, respectively. Even at an extreme high rate of 20 C, it can still release a discharge specific energy of 145.5 Wh kg^{-1}. When the discharge rate is decreased back to 0.05 C, the discharge specific energy could be almost 100% recovered.

4. CONCLUSION

A facile one-pot hydrothermal reaction has been developed to synthesize a precursor of hierarchical micro/nanostructured $MnCO_3$ with olive shape, from which both hierarchical micro/nanostructured MnO and LNMO materials have been prepared through a different calcination process. Thanks to their unique structures, they both show excellent lithium storage properties. The as-synthesized MnO anode in a MnO/Li half cell can deliver a reversible capacity of 782.8 mAh g^{-1} after 200 cycles at 0.13 C and a stable reversible capacity of 350 mAh g^{-1} at a high rate of 2 C. The LNMO cathode in a LNMO/Li half cell can maintain a stable discharge capacity ca. 120.0 mAh g^{-1} in 100 cycles at 0.1 C. Moreover, a lithium ion battery using the MnO as anode and the $LiNi_{0.5}Mn_{1.5}O_{4-\delta}$ as cathode has demonstrated a high discharge specific energy ca. 350 Wh kg^{-1} after 30 cycles at 0.1 C with an average working voltage at 3.5 V and a long cycle stability. After 300 cycles of charge/discharge at a higher rate of 0.5 C, the MnO/$LiNi_{0.5}Mn_{1.5}O_{4-\delta}$ full cell can maintain a discharge specific energy of 227 Wh kg^{-1}. Even at an extreme high rate of 20 C, it can still release a discharge specific energy of 145.5 Wh kg^{-1}. Considering the high specific energy, good cycleability and high rate performance, high safety, and low cost (natural abundance of Mn), the MnO/LNMO full cell demonstrates a potential alternative for the next generation of LIBs. The excellent lithium storage property of the MnO material and its high performance as anode in the MnO/$LiNi_{0.5}Mn_{1.5}O_{4-\delta}$ lithium ion battery is mainly attributed to its hierarchical micro/nanostructure, which could buffer the volume change and shorten the diffusion length of Li^+ during the charge/discharge processes.

■ ASSOCIATED CONTENT

Supporting Information

EIS spectra of commercial MnO, olive MnO/C and pure amorphous carbon electrodes, cycle performance of pure amorphous carbon, schematic diagram and photo of Swagelok type cell, differential capacity curve of MnO/LNMO full cell at a rate of 0.1 C, and cycling performance of the MnO/LNMO full cell at a rate of 0.5 C. This material is available free of charge via the Internet at http://pubs.acs.org.

■ AUTHOR INFORMATION

Corresponding Author

*E-mail: sgsun@xmu.edu.cn.

Notes

The authors declare no competing financial interest.

■ ACKNOWLEDGMENTS

This work is supported by the Special Funds for Major State Basic Research Project of China (2009CB220102, 2011AA11A254), NSFC (21021002), NSFC/HK-RGC Joint Research Scheme (NSFC 20931160426 and N_HKUST609/09), and Xiamen University (20112G003).

■ REFERENCES

(1) Poizot, P.; Laruelle, S.; Grugeon, S.; Dupont, L.; Tarascon, J. M. *Nature* **2000**, *407*, 496−499.
(2) Wu, H. B.; Chen, J. S.; Hng, H. H.; Lou, X. W. *Nanoscale* **2012**, *4*, 2526−2542.
(3) Wang, Z.; Zhou, L.; Lou, X. W. *Adv. Mater.* **2012**, *24*, 1903−1911.
(4) Xu, G. L.; Xu, Y. F.; Sun, H.; Fu, F.; Zheng, X. M.; Huang, L.; Li, J. T.; Yang, S. H.; Sun, S. G. *Chem. Commun.* **2012**, *48*, 8502−8504.
(5) Yu, X. Q.; He, Y.; Sun, J. P.; Tang, K.; Li, H.; Chen, L. Q.; Huang, X. J. *Electrochem. Commun.* **2009**, *11*, 791−794.
(6) Hsiehi, C. T.; Lin, C. C.; Lin, J. Y. *Electrochim. Acta* **2011**, *56*, 8861−8867.

(7) Liu, Y.; Zhao, X.; Li, F.; Xia, D. *Electrochim. Acta* **2011**, *56*, 6448−6452.
(8) Hao, Q.; Xu, L. Q.; Li, G. D.; Ju, Z. C.; Sun, C. H.; Ma, H. Y.; Qian, Y. T. *J. Alloys Compd.* **2011**, *509*, 6217−6221.
(9) Mai, Y. J.; Zhang, D.; Qiao, Y. Q.; Gu, C. D.; Wang, X. L.; Tu, J. P. *J. Power Sources* **2012**, *216*, 201−207.
(10) Zhong, K. F.; Xia, X.; Zhang, B.; Li, H.; Wang, Z. X.; Chen, L. Q. *J. Power Sources* **2010**, *195*, 3300−3308.
(11) Sun, B.; Chen, Z. X.; Kim, H. S.; Ahn, H.; Wang, G. X. *J. Power Sources* **2011**, *196*, 3346−3349.
(12) Ding, Y. L.; Wu, C. Y.; Yu, H. M.; Xie, J.; Cao, G. S.; Zhu, T. J.; Zhao, X. B.; Zeng, Y. W. *Electrochim. Acta* **2011**, *56*, 5844−5848.
(13) Zhong, K.; Zhang, B.; Luo, S.; Wen, W.; Li, H.; Huang, X. J.; Chen, L. Q. *J. Power Sources* **2010**, *196*, 6802−6808.
(14) Zhang, X.; Xing, Z.; Wang, L.; Zhu, Y.; Li, Q.; Liang, J.; Yu, Y.; Huang, T.; Tang, K.; Qian, Y.; Shen, X. *J. Mater. Chem.* **2012**, *22*, 17864−17869.
(15) Li, X. W.; Li, D.; Qiao, L.; Wang, X. H.; Sun, X. L.; Wang, P.; He, D. Y. *J. Mater. Chem.* **2012**, *22*, 9189−9194.
(16) Sun, Y. M.; Hu, X. L.; Luo, W.; Huang, Y. H. *J. Mater. Chem.* **2012**, *22*, 19190−19195.
(17) Luo, W.; Hu, X. L.; Sun, Y. M.; Huang, Y. H. *ACS Appl. Mater. Interfaces* **2013**, *5*, 1997−2003.
(18) Hassoun, J.; Croce, F.; Hong, I.; Scrosati, B. *Electrochem. Commun.* **2011**, *13*, 228−231.
(19) Zhou, L.; Zhao, D. Y.; Lou, X. W. *Angew. Chem., Int. Ed.* **2012**, *51*, 239−241.
(20) Chae, C. J.; Park, H. Y.; Kim, D. w.; Kim, J. S.; Oh, E. S.; Lee, J. K. *J. Power Sources* **2013**, in press.
(21) Qiu, Y. C.; Xu, G. L.; Yan, K. Y.; Sun, H.; Xiao, J. W.; Yang, S. H.; Sun, S. G.; Jin, L. M.; Deng, H. *J. Mater. Chem.* **2011**, *21*, 6346−6353.
(22) Yu, Y.; Chen, C. H.; Shui, J. L.; Xie, S. *Angew. Chem., Int. Ed.* **2005**, *44*, 7085−7089.
(23) Xu, G. L.; Li, J. T.; Huang, L.; Lin, W. F.; Sun, S. G. *Nano Energy* **2013**, *2*, 394−402.
(24) Wang, Z. Y.; Luan, D. Y.; Madhavi, S.; Li, C. M.; Lou, X. W. *Chem. Commun.* **2011**, *47*, 8061−8063.
(25) He, Y.; Huang, L.; Cai, J. S.; Zheng, X. M.; Sun, S. G. *Electrochim. Acta* **2010**, *55*, 1140−1144.
(26) Wang, X.; Li, X.; Sun, X.; Li, F.; Liu, Q.; Wang, Q.; He, D. *J. Mater. Chem.* **2011**, *21*, 3571−3573.
(27) Ke, F. S.; Huang, L.; Wei, G. Z.; Xue, L. J.; Li, J. T.; Zhang, B.; Chen, S. R.; Fan, X. Y.; Sun, S. G. *Electrochim. Acta* **2009**, *54*, 5825−5829.
(28) Zhang, K. J.; Han, P. X.; Gu, L.; Zhang, L. X.; Liu, Z. H.; Kong, Q. S.; Zhang, C. J.; Dong, S. M.; Zhang, Z. Y.; Yao, J. H.; Xu, H. X.; Cui, G. L.; Chen, L. Q. *ACS Appl. Mater. Interfaces* **2012**, *4*, 658−664.
(29) Laruelle, S.; Grugeon, S.; Poizot, P.; Dolle, M.; Dupont, L.; Tarascon, J. M. *J. Electrochem. Soc.* **2002**, *149*, A627−A634.
(30) Xiao, J.; Chen, X. L.; Sushko, P. V.; Sushko, M. L.; Kovarik, L.; Feng, J. J.; Deng, Z. Q.; Zheng, J. M.; Graff, G. L.; Nie, Z. M.; Choi, D. W.; Liu, J.; Zhang, J. G.; Whittingham, M. S. *Adv. Mater.* **2012**, *24*, 2109−2116.
(31) Fu, F.; Xu, G. L.; Wang, Q.; Deng, Y. P.; Li, X.; Li, J. T.; Huang, L.; Sun, S. G. *J. Mater. Chem. A* **2013**, *1*, 3860−3864.
(32) Yang, Y.; McDowell, M. T.; Jackson, A.; Cha, J. J.; Hong, S. S.; Cui, Y. *Nano Lett.* **2010**, *10*, 1486−1491.